J. Fluid Mech. (1992), *vol.* 239, *pp.* 461–488
Printed in Great Britain

Microburst modelling and scaling

By T. S. LUNDGREN[1], J. YAO[1] AND N. N. MANSOUR[2]

[1] Department of Aerospace Engineering and Mechanics, University of Minnesota, Minneapolis, MN 55455, USA

[2] NASA Ames Research Center, Moffett Field, CA 94035, USA

(Received 14 March 1991 and in revised form 6 December 1991)

A microburst can be modelled by releasing a volume of fluid that is slightly heavier than the ambient fluid, allowing it to fall onto a horizontal surface. Vorticity develops on the sides of this parcel as it descends and causes it to roll up into a turbulent vortex ring which impinges on the ground. Such a model exhibits many of the features of naturally occurring microbursts which are a hazard to aviation. In this paper this model is achieved experimentally by releasing a volume of salt water into fresh water from a cylindrical dispenser. When care is taken with the release the spreading rate of the surface outflow is measurable and quite repeatable despite the fact that the flow is turbulent. An elementary numerical approximation to this model, based on inviscid vortex dynamics, has also been developed. A scaling law is proposed which allows experiments with different fluid densities to be compared with each other and with the numerical results. More importantly the scaling law allows us to compare the model results with real microbursts.

1. Introduction

Downbursts are wind systems, potentially hazardous to aircraft, which occur when downdraughts, caused by rapid evaporation, melting and precipitation drag, fall to Earth and spread outward along the surface. When aircraft fly through such a structure, on take off or landing, the rapidly varying horizontal wind velocities (windshear) can cause accidents unless proper strategy is followed. Fujita (1985, 1986) has written several books documenting this phenomenon, and has invented the words 'downburst' and 'microburst' to describe it (Fujita 1981). The term microburst refers to an intense downburst with horizontal extent less than 4 km, the scale felt to be most dangerous to aircraft. Proctor (1988) presented large-scale numerical simulations which included turbulence modelling and cloud microphysics.

In this paper we present a simple microburst model which can be approximated numerically and created in a laboratory experiment. A volume of fluid which is slightly heavier than its surroundings is released to fall onto a horizontal surface. This provides an experimentally repeatable laboratory microburst. Scorer (1957) modelled thermals in this way, without the ground effect. A laboratory microburst such as this has been photographed by Fujita (1985), but we are not aware of any quantitative measurements. Clearly the model does not include the many complex meteorological factors which cause an intense local downdraught to occur. The real causes of the phenomenon make microbursts extremely variable and therefore not easily amenable to laboratory investigation. We hope to extract some of the features common to all microbursts with this model. We will compare experiments with the results of an elementary numerical model which approximates the physical situation.

Our numerical model is similar to one used by Dahm, Scheil & Tryggvason (1989) in their experimental and numerical study of vortex interaction with a density interface.

Elementary models have been developed by Ivan (1986) and Zhu & Etkin (1985) which are of value to engineers developing avoidance strategies and detection schemes. These consist of a *stationary* vortex ring and dipole disk, respectively. Since a microburst can change considerably during the time it takes an airplane to traverse it we feel there is a need for a simple dynamical model which captures the essential physics of the process and can be realistically scaled to represent a full size microburst. We stress that we want an elementary (and economical) model for this purpose.

In the simplest kind of mathematical modelling of an idealized microburst we neglect diffusion between the heavier and lighter fluids so there is always a sharp density discontinuity across the separating interface; mixing consists only of gross folding and rolling-up of the interface. We assume that the fluid is incompressible and that the density difference $\Delta\rho$ is small enough to use the Boussinesq approximation. The appropriate non-viscous equations are

$$\nabla \cdot \boldsymbol{u} = 0, \tag{1.1}$$

$$\frac{\mathrm{d}\boldsymbol{u}}{\mathrm{d}t} = -\frac{\nabla p}{\rho} - g\frac{\rho'}{\rho}\hat{\boldsymbol{k}}, \tag{1.2}$$

where ρ' is zero in the lighter fluid and equal to $\Delta\rho$ in the downburst parcel. The small number of parameters in the problem can be absorbed by changing variables. As a characteristic length we use the equivalent spherical radius R_0 of the downburst parcel, and we introduce a characteristic time

$$T_0 = \left(\frac{R_0\rho}{g\Delta\rho}\right)^{\frac{1}{2}}. \tag{1.3}$$

All lengths are made dimensionless with R_0, time is made dimensionless with T_0, and velocity is made dimensionless with $V_0 = R_0/T_0$. Using the same notation for the dimensionless variables, we have

$$\nabla \cdot \boldsymbol{u} = 0, \tag{1.4}$$

$$\frac{\mathrm{d}\boldsymbol{u}}{\mathrm{d}t} = -\nabla p - I\hat{\boldsymbol{k}}, \tag{1.5}$$

where I is unity in the microburst material and zero elsewhere. Therefore all physical variables have been absorbed into the length- and timescales. This almost trivial result, which we believe to be a new idea in this context, gives an important scaling law which relates model studies to full-scale microbursts. We can easily compare numerical results with experimental model results taken with different values of R_0 and $\Delta\rho$ since we can construct the length- and timescales required for dimensionless presentation. We have only to require geometrical similarity of the compared flows. To compare with real microbursts it is necessary to establish effective values of R_0 and T_0 indirectly, from aircraft flight recorders and meterological Doppler radar data. Here the value is in being able to realistically calibrate the numerical model in order to use it for the study of aircraft survival strategies.

There is also a possible dependence on a Reynolds number defined by

$$Re = \frac{R_0 V_0}{\nu}; \tag{1.6}$$

however, large-scale turbulent flows are only weakly dependent on Reynolds number. As will be seen we find Reynolds-number dependence in the model experimental data only at the lowest *Re* values, i.e. at small values of $\Delta\rho$.

Density stratification of the ambient atmosphere introduces another possibly important parameter. While this effect could be studied by constructing salt stratification in our experimental tank we have decided not to include these complications in the present study. This decision is partly based on the knowledge that the Dallas-Fort Worth microburst, to which we refer later, occurred under neutrally stable conditions as shown by nearby meteorological surroundings.

It is useful here to give a discussion of the similarities and differences between turbulent vortex rings and thermals since our microburst mode resembles the latter until it is modified by interaction with the ground.

Vortex rings are produced experimentally by pushing a slug of fluid from a cylinder or through a hole in a flat plate by moving a piston. A vortex ring rolls up from the shear layer which accompanies the slug and is developed by the time the slug moves about a diameter. The circulation Γ is approximately the piston speed times the distance it moves. Maxworthy (1972, 1974) showed that the ring becomes turbulent when the Reynolds number Γ/ν is greater than about 600, and not only is the vortex core turbulent but an ellipsoidal 'bubble' of fluid moving with the vortex ring is also turbulent. Maxworthy gave experimental support to the following physical picture. The comoving turbulent bubble entrains non-turbulent fluid into its front and ejects most of it into a wake along with some of the vorticity of the ring. A small amount of the entrained fluid is retained causing the ring core and bubble to slowly increase in size. The loss of circulation to the wake slows the vortex down, halving the initial velocity by the time it has travelled about 10 initial diameters. Maxworthy estimated the effective drag coefficient based on the projected area of the bubble to be about 0.04.

In Scorer's (1957) thermal model, and in our microburst model, a parcel of heavier fluid is dropped from rest into a surrounding lighter fluid and develops into a vortex ring through baroclinic vorticity generation by the time it has fallen a diameter or less. It is clear from Scorer's photographs (and our figure 1*a*) that the comoving fluid bubble is turbulent. Because of the weight of the fluid there are important differences from a constant-density vortex flow. There is entrainment into the front of the bubble but very little wake. The fluid which is entrained at the front swirls back around the vortex core from the rear causing the vortex core radius and the size of the bubble to increase. Further, because very little vorticity is lost to a wake the circulation stays constant. Scorer's study of the flow pattern in a thermal and his photograph from the rear of a model thermal showing a hollowed-out region of clear fluid at the centre of the vortex ring both support this conclusion. The velocity of a vortex ring is proportional to the circulation and inversely proportional to the radius of the ring. Therefore the velocity of the falling parcel increases at first as the heavier fluid accelerates. It reaches a nearly constant velocity as the circulation becomes fully developed and then gradually slows down as the vortex ring and bubble increase in size. Whereas the turbulent vortex ring slows down because of loss of circulation, the turbulent thermal slows down because it gets larger.

Turner (1957) analysed the growth of a constant-circulation buoyant vortex ring in terms of its impulse (essentially its momentum) by means of the simple formula

$$\frac{\mathrm{d}P}{\mathrm{d}t} = W, \tag{1.7}$$

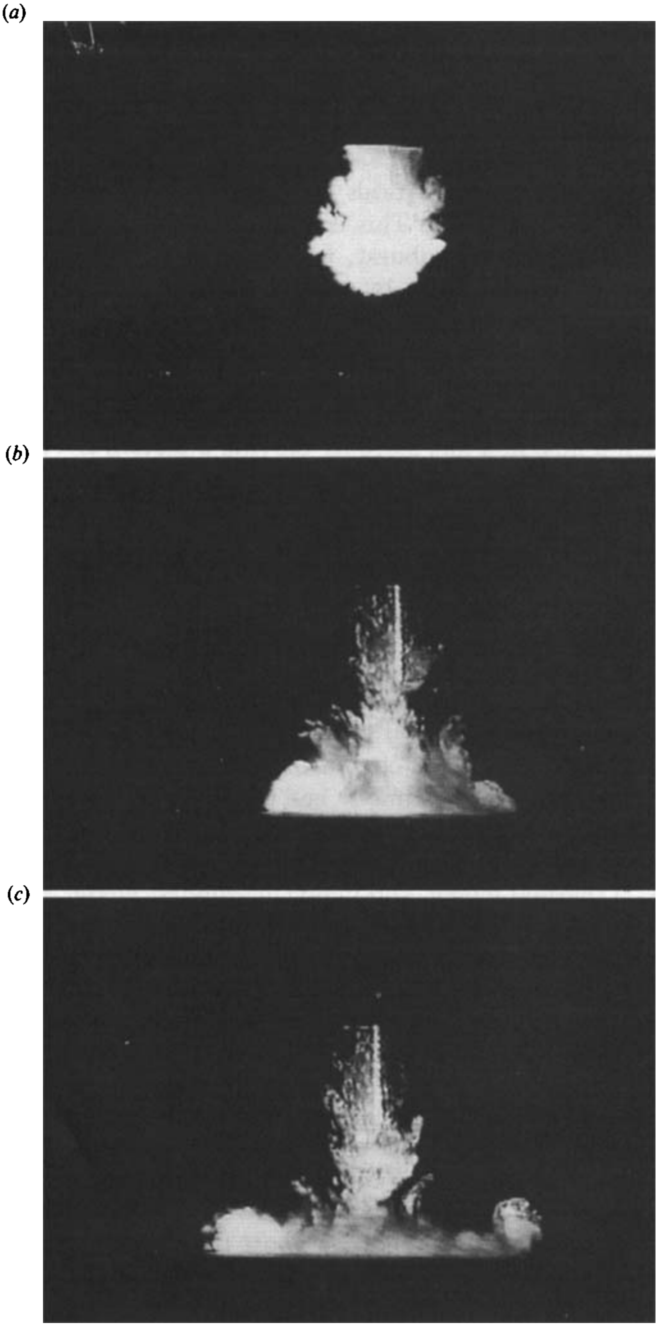

FIGURE 1 (*a–c*). For caption see facing page.

where $P = \pi\rho\Gamma R^2$ is the impulse, W is the constant weight of the vortex ring and its comoving bubble and R is the ring radius. This leads to Turner's result

$$R^2 = R_0^2 + \frac{W}{\pi\rho\Gamma}t. \tag{1.8}$$

In order for the impulse to increase, as (1.7) demands, without increasing the velocity, the mass of the turbulent bubble must increase.

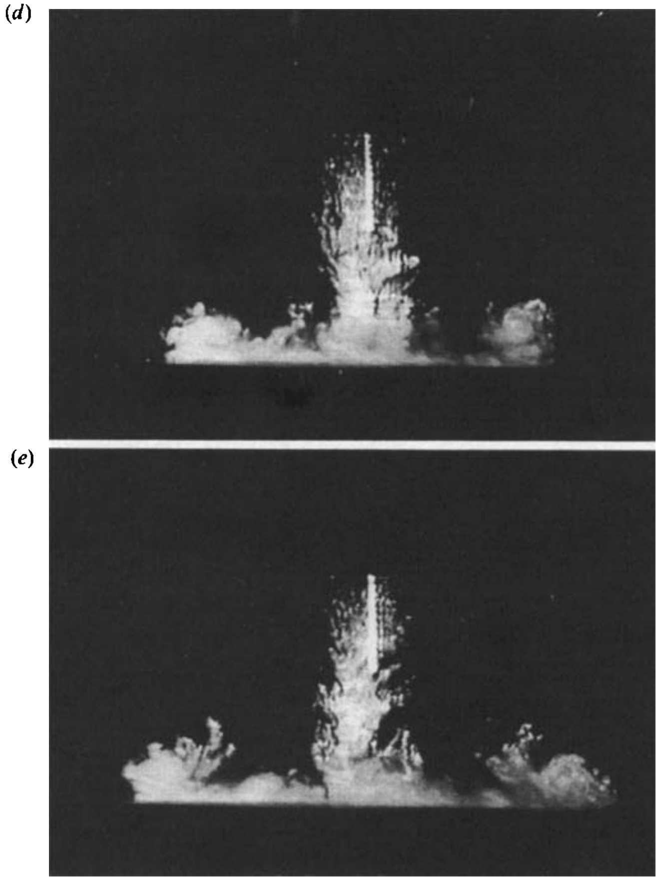

FIGURE 1. Simulated microburst. $\Delta\rho/\rho = 0.03$, 4 in. release. Approximate times from release T/T_0; (*a*) 3; (*b*) 6.5; (*c*) 8; (*d*) 9; (*e*) 11.5.

If we modify Turner's formula to

$$\frac{\mathrm{d}P}{\mathrm{d}t} = W - D, \tag{1.9}$$

where D is the drag, and estimate the drag by using Maxworthy's drag coefficient (we believe the drag coefficient is actually much smaller than this) we find that the drag is less than 1% of the weight and therefore quite negligible anyway.

Our experimental set-up is described and the experimental results are shown in §2 and the numerical model is presented in detail in §3 and compared with real microbursts in §4.

2. Experimental arrangement and results for a simulated microburst

A salt-water solution containing Kaliroscope (crystaline platelets, approximately 10^{-5} cm thick and 10^{-3} cm across) or laser-fluorescent dye, or both, for visualization, is dropped into fresh water from a cylindrical container onto a raised circular 20 in. diameter glass plate which simulates the ground. The cylinder and plate are contained in a glass-walled tank, 2 ft on a side, filled with about 12 in. of water above

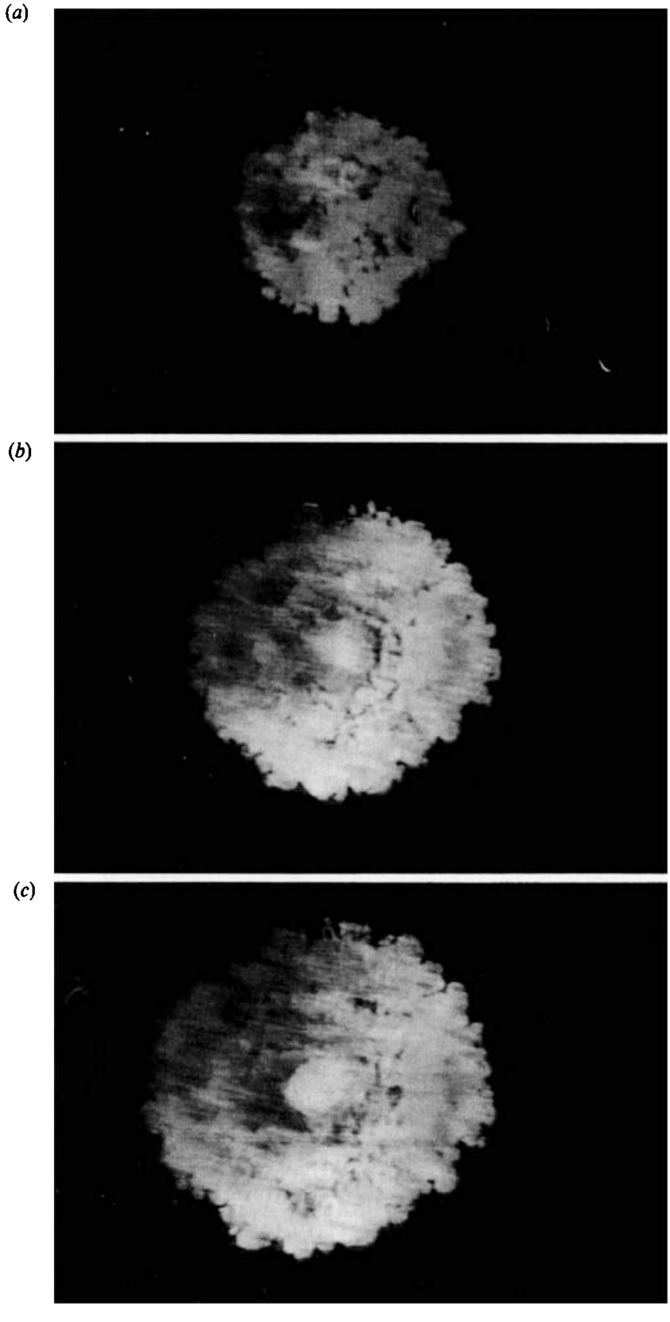

FIGURE 2. Bottom view of simulated microburst. $\Delta\rho/\rho = 0.03$, 4 in. release. Approximate times from release: (*a*) 11.0; (*b*) 18.2; (*c*) 22.5.

the plate. The cylinder is plastic with solid walls, open at the bottom and drilled at the top to about 50% solidity. The cylinder is held rigidly from above by a hollow rod. We cover the open end of the cylinder with a thin stretched latex sheet, fill it with salt water of the desired density, and carefully burst the latex sheet with a needle inserted from above through the hollow support rod. The simulated microburst is illuminated from the side by either a high-intensity laser sheet or by

Identifier	$\Delta\rho/\rho$	R_0((mm)	T_0(s)	Re
V10301	0.01	26.66	0.516	1377
V10303	0.03	26.66	0.298	2385
V10305	0.05	26.66	0.231	3077
V10310	0.10	26.66	0.163	4360
V20305	0.05	33.99	0.261	4427
V20310	0.10	33.99	0.184	6279
V10405	0.05	26.66	0.231	3077
V10410	0.10	26.66	0.163	4360
V20405	0.05	33.99	0.261	4427
V20410	0.10	33.99	0.184	6279

TABLE 1. The experimental cases studied

a bright incandescent light, depending on the desired effect, and the event is recorded by video camera. The microburst takes the form of a descending vortex ring which flows outward along the surface and finally runs off the edge of the circular glass plate, draining the heavier liquid into the space below the plate. To minimize edge effects we make observations only while the microburst front is within 7 in. of the centre of the plate. After four runs the tank is drained, cleaned and refilled.

The main cylindrical container has a 45 mm inside diameter and a 45 mm inside height. The cylinder is filled slowly through a thin tube while in place above the plate. For definiteness it is filled to the top of the drilled holes. Including a small correction for the volume of the drilled holes, the equivalent spherical radius of the dropped volume is $R_0 = 26.66$ mm. A second, larger cylinder is geometrically similar with $R_0 = 33.99$ mm. In two series of experiments presented here we place the bottom of the cylinder a distance $H_0 = 2.86\,R_0$ and $H_0 = 3.81\,R_0$ above the glass plate. (These heights are 3 in. and 4 in. respectively, for the smaller cylinder.)

Figure 1 shows a typical experiment, photographed from the television monitor. This is from the 4 in. series with $\Delta\rho/\rho = 0.03$, and it is illuminated by laser light. The approximate dimensionless times after release are shown in the figure caption. The sense of rotation in the vortex ring gives outward velocities near the ground, a clockwise sense in the left half of the figures. Vorticity with the opposite circulation (counter-vorticity) is generated by friction with the ground. Counter-vorticity is swept upward along the front of the vortex. This can be seen as the small surface features in figures 1 (*c–e*). The sense of rotation of these surface swirls is clearer in the action video. The visually apparent slowly descending central column is exaggerated by the laser illumination of dye which remains from the starting process, not much of the salt water remains in this location. This effect is not so visible with incandescent lighting.

Figure 2 shows a sequence of views from below, using a 45° mirror and illumination by a horizontal laser sheet just above the glass surface. Dye is used for visualization. This shows fairly good axial symmetry, but with pronounced petal-like lobes along the gust front. This interesting feature has not previously been reported for microbursts, but a similar effect has been observed at the front of gravity currents and has been explained by Simpson (1972) to be due to a convective instability of a thin layer of light fluid which has been overrun by the heavy fluid.

Quantitative results have been obtained from the video records of a number of microburst releases by using a digitizing cursor on the television monitor. The quantities measured were the maximum radius R of the microburst image (half the

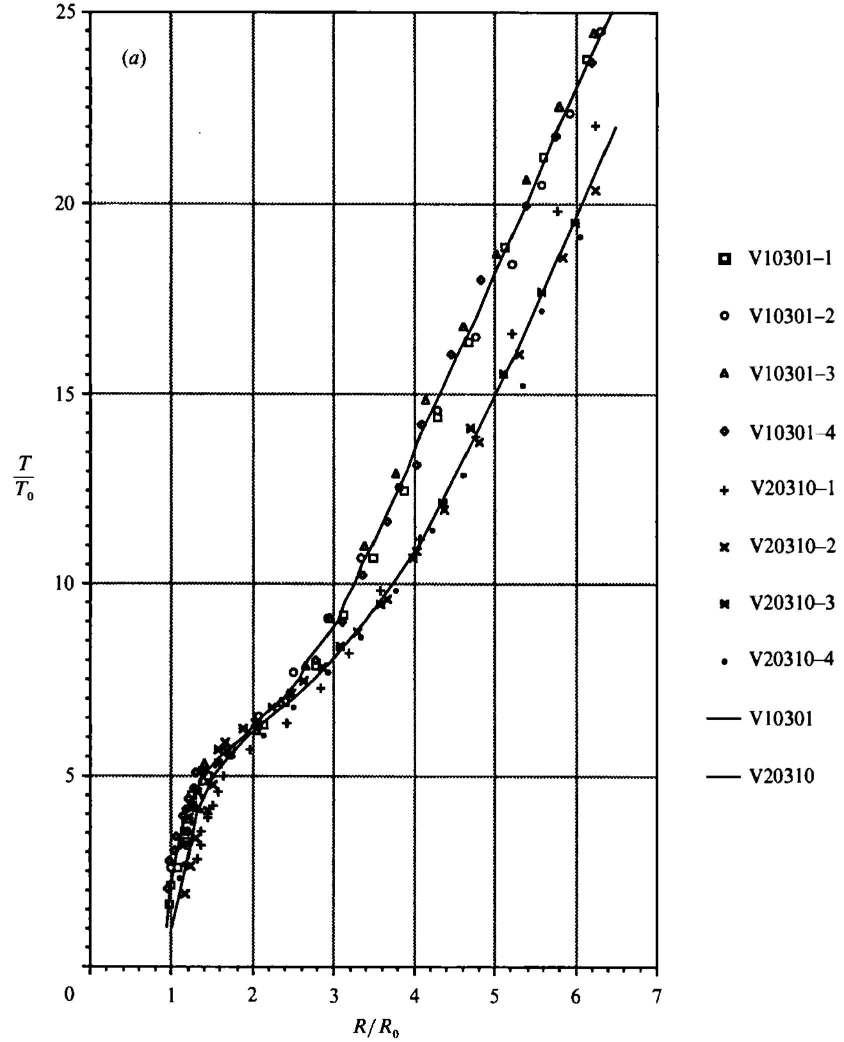

FIGURE 3(a). For caption see facing page.

apparent diameter) and its minimum distance H above the ground. These quantities have been presented as R/R_0 and H/R_0 versus T/T_0, where R_0 and T_0 are the length- and timescales defined in §1. The first objective is to show that the results are independent of Reynolds number (for large Reynolds number) when presented in this dimensionless form.

Table 1 identifies all of the experimental cases. In the identifier column V1 or V2 refer to the small or large cylinder, 03 or 04 are the 3 in. or 4 in. series, and the last two digits are $\Delta\rho/\rho$ for the salt solution (01 means $\Delta\rho/\rho = 0.01$). When the large cylinder is used we still refer to the experiments as the 3 in or 4 in. series, but the initial height is actually larger by the ratio of the lengthscales of the cylinders.

Figure 3(a) presents R/R_0 versus T/T_0 for the 3 in. series for the smallest and largest Reynolds number showing all the data from 4 runs with each Reynolds number, identifying each run by a different marker to show how well the experiments can be repeated. The curves are least-squares fits to each set of 4 runs. Figure 3(b)

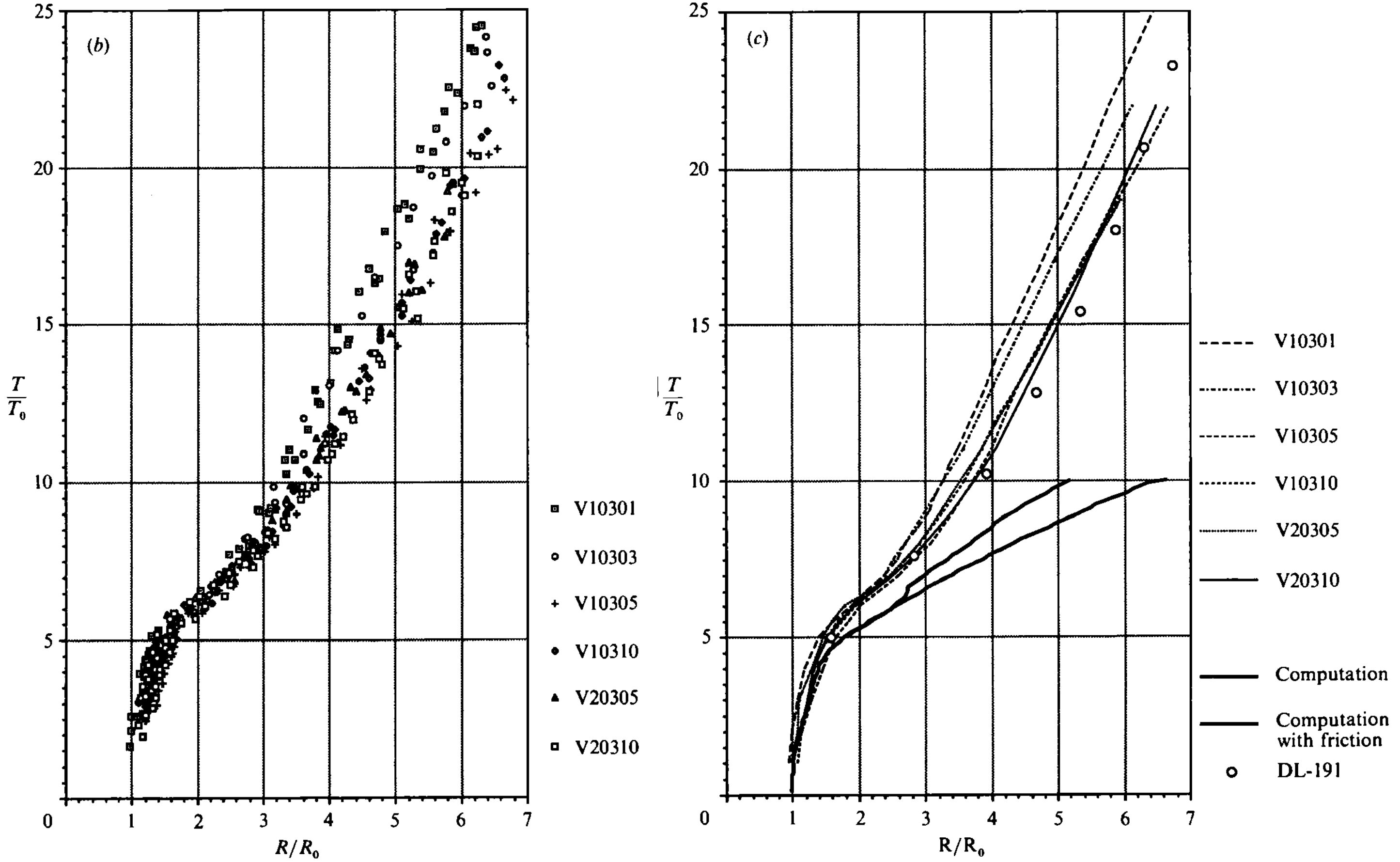

FIGURE 3. Maximum radius of simulated microburst versus time, 3 in. release. (*a*) Upper curve is least-squares fit to data from 4 runs with $\Delta\rho/\rho = 0.01$, lower curve for $\rho/\rho = 0.1$; (*b*). All 3 in. data. (*c*) Least squares fit to 3 in. data compared with results of computations and Dallas–Fort Worth microburst event (DL 191). $H/R_0 = 2.85$.

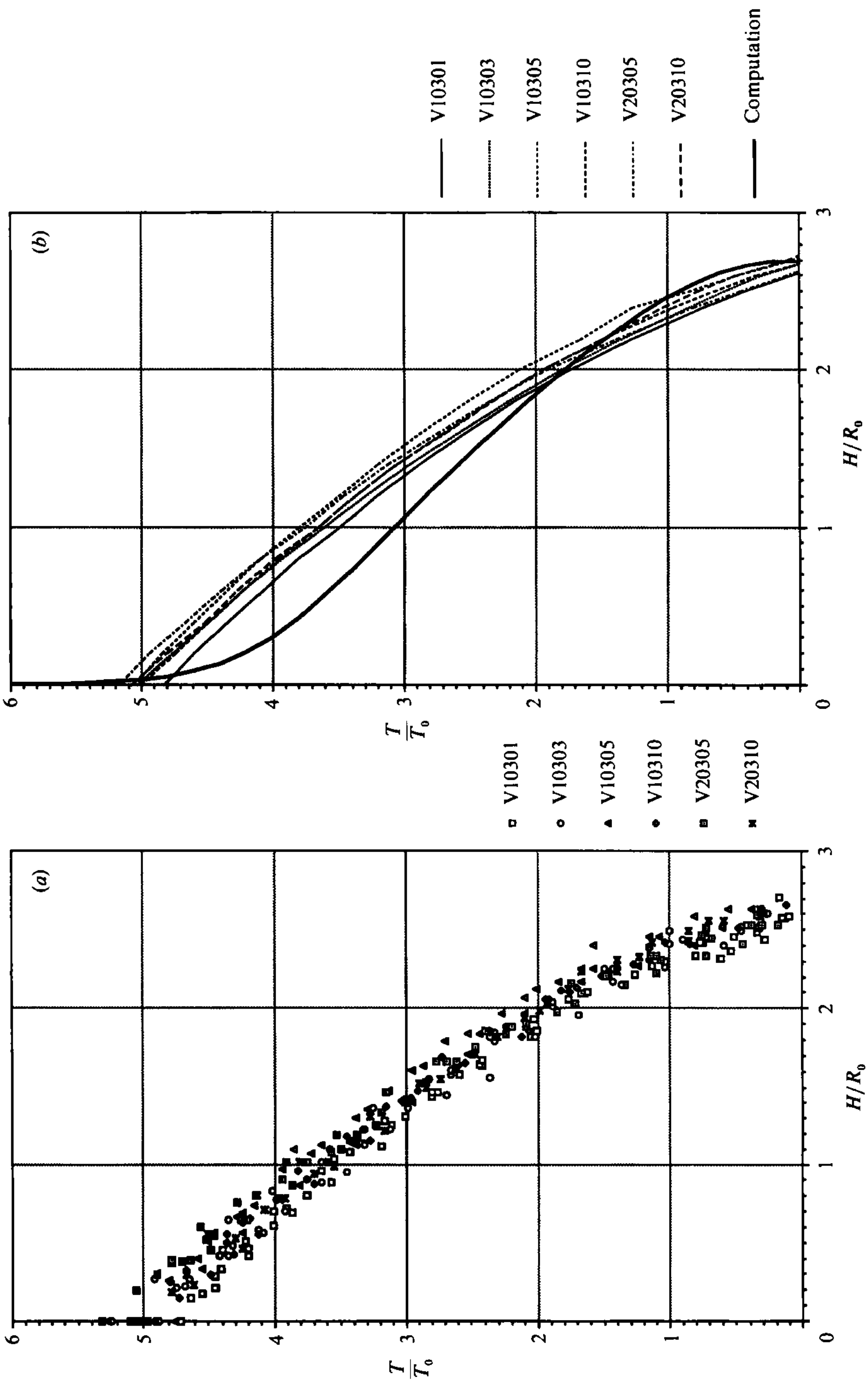

FIGURE 4. Distance from bottom of simulated microburst to the ground versus time, 3 in. release. (*a*) All 3 in. data; (*b*) least-squares fits compared with computation.

FIGURE 4. (Landscape)

shows all the 3 in. series data with one marker for each set of four runs in each of the six Reynolds number categories. There is a clear Reynolds number effect for low values of the Reynolds number with the results becoming independent of Reynolds number for large values. Figure 3(*c*) contains least-squares fits to the data from figure 3(*b*), and the data points are omitted in order to more clearly see the Reynolds-number trend. The figure also contains the results from computations which will be described in the next section. The open circles are data points from the DL 191 microburst which occurred at Dallas–Fort Worth airport on 2 August 1985. These data were obtained from Fujita (1986, figure 5.9). The length- and timescales used were $L_0 = 0.7$ km and $T_0 = 23$ s, determined so that the two earliest data points agree with the 3 in. data. This establishes the scaling for DL 191.

Figure 4 shows H/R_0 versus T/T_0 for the 3 in. series. Figure 4(*a*) contains all the data and figure 4(*b*) compares least-squares fits to the data to the result from the numerical simulation. There is no definite trend with Reynolds number in this case, only scatter. The experimental microbursts accelerate at first and reach a nearly constant velocity by the time they have fallen about half a diameter, as was discussed in the introduction. We interpret this to mean that the circulation has become fully developed by this time. We will show a computation of developing circulation later.

Figures 5 and 6 show the 4 in. series data in a similar manner except that we do not show the two smallest Reynolds numbers. The open circles from DL 191 in figure 5(*b*) are the same data points shown in figure 3(*c*) shifted up by one time unit because touchdown was at $T/T_0 = 6$ for the 4 in. data and at $T/T_0 = 5$ for the 3 in. data.

An overview of both sets of radius data shows that before touchdown the microburst radius spreads approximately linearly with time with a speed of about $0.16V_0$. After touchdown the gust front accelerates at first to a maximum radial velocity of about $0.5V_0$ and then decelerates to a nearly constant velocity of about $0.2V_0$. The maximum spreading rate occurs about one time unit after touchdown.

Are the DL 191 scalings ($T_0 = 23\,\mathrm{s}, R_0 = 0.7$ km) reasonable? We note that the 3 in. and 4 in. release heights correspond to 6600 ft and 8800 ft in the DL 191 context. Either of these seems appropriate in the light of a 6000 ft cloud base at the time of this microburst. The times from release to touchdown of $T = 5T_0$ and $T = 6T_0$ for the 3 in. and 4 in. data correspond to 1.9 min and 2.3 min, respectively. These values are consistent with the rapidly changing sequences of events described by Fujita (1986), in which the microburst descended about 4000 ft in the minute before touchdown and resulted in the airplane crash two minutes later.

Some comments are in order here regarding the comparison of these measurements with the computations. It is apparent from figures 4 and 6 that the numerical microburst descends faster than the experiments and from figures 3 and 5 that the numerical gust front spreads faster along the ground than do the experiments. This occurs because of a difference in the initial conditions. The experimental microburst is dropped from a cylindrical container, while the numerical microburst is started by releasing a spherical volume. We have tried different initial shapes and have found that if the released parcel is flatter on the bottom it falls slower. If the initial radius is $0.999+0.1P_3(\cos\theta)$ (P_3 is a Legendre polynomial, θ the polar angle), which is a little flatter on the bottom and slightly pointed on the top, the numerical descent agrees almost perfectly with figures 4 and 6. It falls more slowly because the circulation that develops is about 10% less. Furthermore this same initial condition causes much better agreement between the numerical gust front and the experiments in figures 3 and 5. We have chosen to use the spherical initial condition throughout

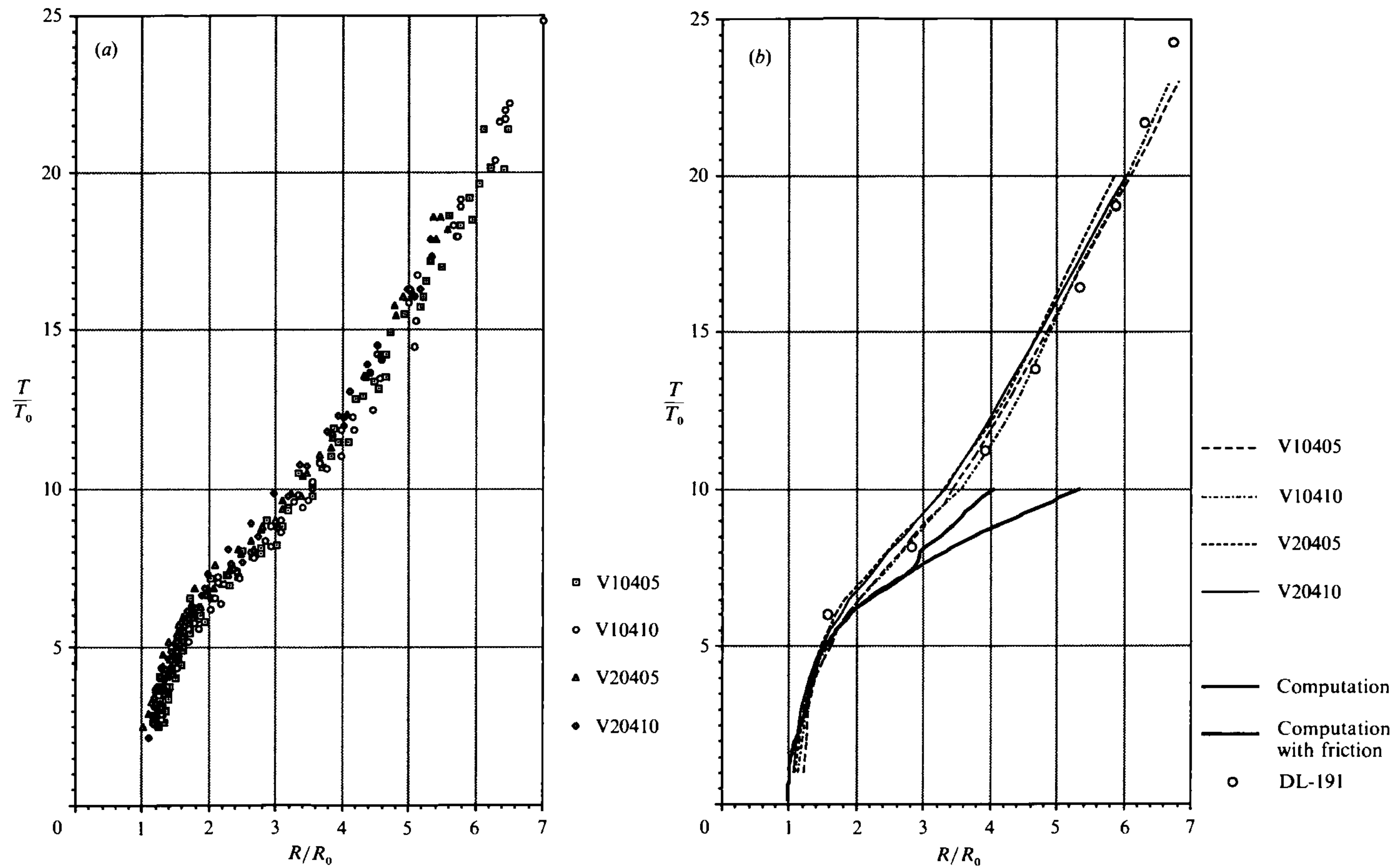

FIGURE 5. Maximum radius of simulated microburst versus time, 4 in. release. (*a*) All 4 in. data, (*b*) Least-squares fits to 4 in. data compared with computations and Dallas–Fort Worth microburst event. $H/R_0 = 3.81$.

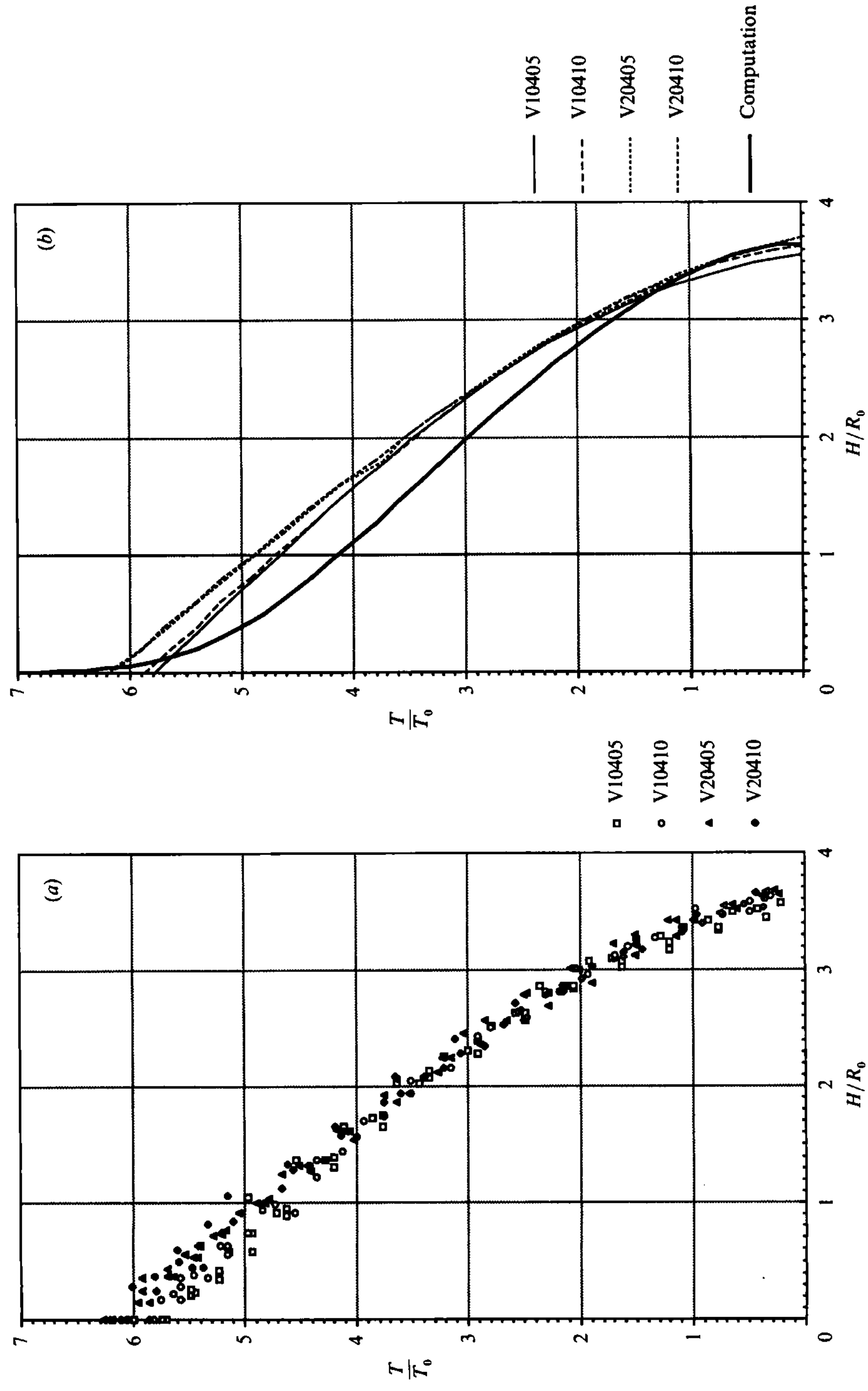

FIGURE 6. Same as figure 4 but with 4 in. release.

this paper because it seems improper to fine tune such a model. When calibrating the model for aerodynamic use we would use microburst observations near the ground to set the appropriate scaling. The exact initial conditions are then less relevant.

3. Numerical microburst model

The Biot–Savart law represents the velocity field as an integral over the vorticity field. In our case the flow is irrotational except for vorticity concentrated in a vortex sheet at the interface between the heavier fluid parcel and the ambient surroundings plus a mirror-image vortex sheet below the ground to satisfy the impenetrability condition. Because the flow is axially symmetric the vortex sheet is a smooth distribution of vortex rings centred on the axis, and the velocity can be expressed in the form

$$u_r(r,z,t) = \int U_r(r,z;r',z')\,\gamma(s',t)\,\mathrm{d}s', \tag{3.1}$$

$$u_z(r,z,t) = \int U_z(r,z;r',z')\,\gamma(s',t)\,\mathrm{d}s', \tag{3.2}$$

where U_r and U_z are the radial and axial velocity components at the field point r, z due to a vortex ring of unit circulation through the integration point r', z'. The integration variable is arclength along the intersection of the surface with a meridian plane. We picture the meridian plane in the left half of the intersection plane with integration from the top centre of the parcel boundary to the bottom centre (a counter-clockwise sense), plus the image integration. The function γ is the circulation density (counter-clockwise circulation is positive) at the integration point. The functions U_r and U_z can be deduced from the stream function for a vortex ring given by Lamb (1932, section 161). They depend on elliptic integrals, which fortunately can be approximated by algebraic and logarithmic functions with suitable accuracy (Abramowitz & Stegun 1972).

From (3.1) and (3.2) we can compute the velocity at any point in the field, in particular on either side of the interface. (The integrals are singular at the interface. If they are interpreted as principal-value integrals we will automatically compute the average velocity at the interface. However, it is necessary to desingularize the integral for mathematical reasons. This will be explained below.)

The circulation density function can be determined from the Bernoulli equation by matching the pressures across the interface by

$$\rho_1\left(\frac{\partial\phi_1}{\partial t}+\frac{\boldsymbol{u}_1\cdot\boldsymbol{u}_1}{2}+gz\right) = \rho_2\left(\frac{\partial\phi_2}{\partial t}+\frac{\boldsymbol{u}_2\cdot\boldsymbol{u}_2}{2}+gz\right), \tag{3.3}$$

where subscript 1 indicates a point on the heavy fluid side of the interface and subscript 2 a point just across the interface on the ambient side. In the Boussinesq approximation (g large, $\Delta\rho = \rho_1-\rho_2$ small) this gives

$$\frac{\partial(\phi_1-\phi_2)}{\partial t}+\frac{(\boldsymbol{u}_1-\boldsymbol{u}_2)\cdot(\boldsymbol{u}_1+\boldsymbol{u}_2)}{2}+g\frac{\Delta\rho}{\rho}z = 0, \tag{3.4}$$

which may be written

$$\frac{\mathrm{d}\mu}{\mathrm{d}t} = -g\frac{\Delta\rho}{\rho}z, \quad \mu = \phi_1 - \phi_2, \tag{3.5}$$

where the straight derivative follows the average velocity of the interface, i.e.

$$\frac{\mathrm{d}}{\mathrm{d}t} = \frac{\partial}{\partial t} + \frac{(\boldsymbol{u}_1 + \boldsymbol{u}_2)}{2}\cdot\boldsymbol{\nabla}. \tag{3.6}$$

The circulation density is related to the dipole density μ by

$$\gamma = -\frac{\partial\mu}{\partial s}. \tag{3.7}$$

The dimensionless scheme proposed in the introduction is effectively implemented by setting the initial spherical radius of the parcel to unity and taking $g\Delta\rho/\rho = 1$.

Lagrangian nodal points are placed along the interface, the first and last points being on the axis. We introduce an index function ξ, which takes integer values at the nodes as an integration variable in place of s, using

$$\frac{\partial\mu}{\partial s}\mathrm{d}s = \frac{\partial\mu}{\partial\xi}\mathrm{d}\xi \tag{3.8}$$

and approximate the integral by a midpoint formula, using a fourth-order-accurate interpolation formula to establish the midpoint values. The numerical strategy is to compute the average velocities at the nodal points from (3.1) and (3.2), update each nodal position $\boldsymbol{r}$ by

$$\frac{\mathrm{d}\boldsymbol{r}}{\mathrm{d}t} = \frac{\boldsymbol{u}_1 + \boldsymbol{u}_2}{2} \tag{3.9}$$

and use (3.5) to update μ. Then $\partial\mu/\partial\xi$ can be computed by a fourth-order-accurate Padé approximate formula, to set the stage for the next time step. A fourth-order Runge–Kutta scheme is used for time advancement.

The strategy just described will ultimately fail. Vortex sheets are extremely unstable with a growth rate which becomes infinite as the wavelength of a disturbance tends to zero. This leads to the appearance of mathematical roll-up singularities (not merely numerical instabilities) which develop in a finite time. This effect has been studied by Moore (1979), Meiron, Baker & Orszag (1982) and Higdon & Pozrikidis (1985). This situation can be avoided by allowing the vortex sheet to have a finite thickness. This can be done in several ways. In a physical approach to the problem Pozrikidis & Higdon (1985) have studied the evolution of thin vortex layers of uniform vorticity. This prevents a singularity by developing a pronounced elliptical bulge on the layer at the place where an infinitesimal sheet would develop a singular concentration of vorticity. Effectively, it develops a vortex with a finite core. Another approach, which we will adopt, is to desingularize the kernels in (3.1) and (3.2) so that they look like the velocity components of a vortex with a finite core, a vortex blob (Leonard 1985) instead of a point vortex. Krasny (1987) has studied this method in detail, for two-dimensional problems, as the size of the vortex blob tends to zero. Tryggvason (1989) has compared vortex-blob computations with vortex-in-cell computations which effectively give the vortex sheet a finite thickness because of the finite spacing of the numerical mesh. He showed that similar numerical results are obtained by the two methods when the blob size and the mesh

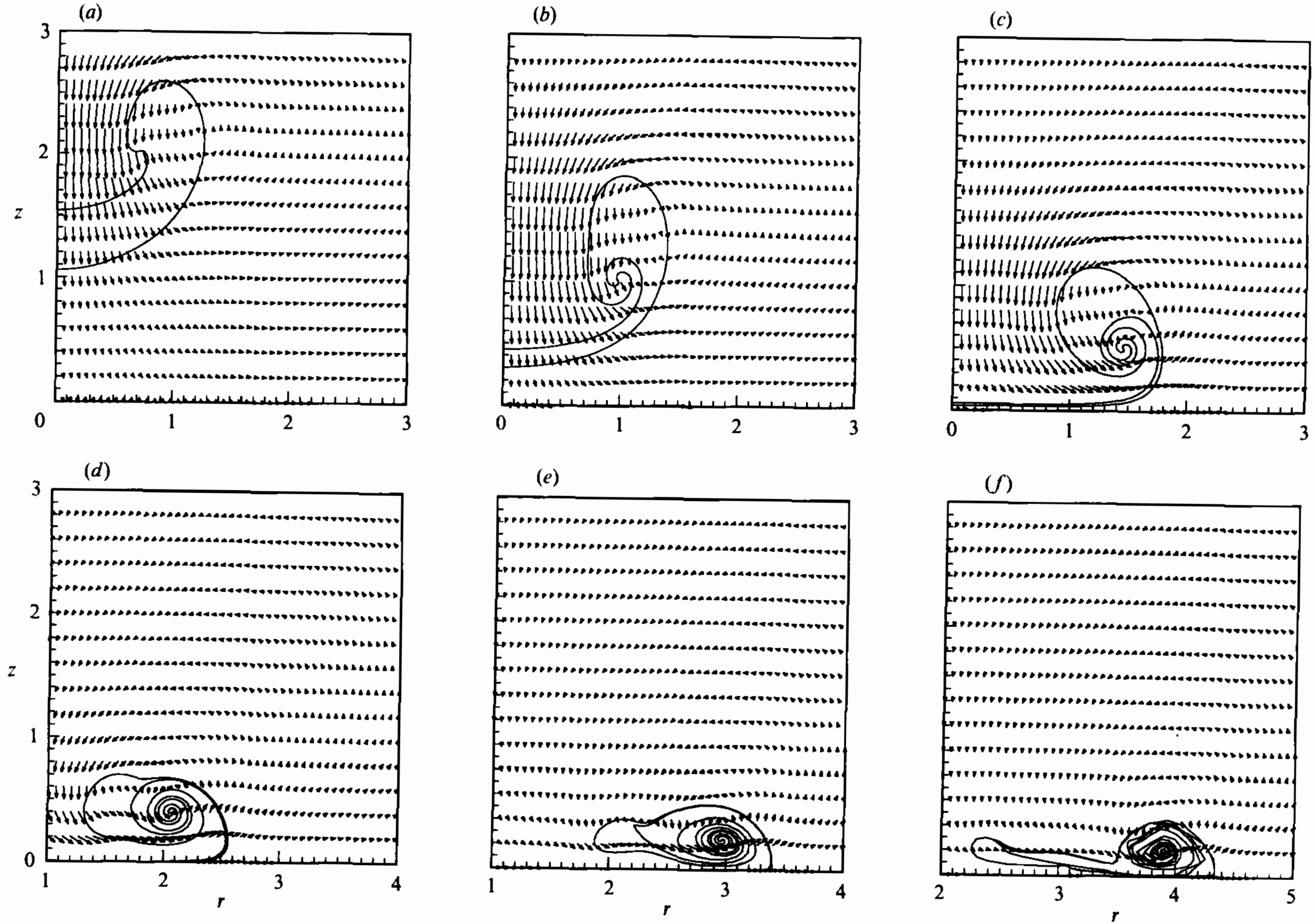

FIGURE 7. Vector plots of numerical microburst, $\delta = 0.15$. Velocity scale is 0.1 (distance between ticks). Contour is interface between heavier and lighter fluids. Initial shape is a sphere with centre of gravity at 3.71 units (corresponding to the 3 in. series of experiments). (*a*) $T/T_0 = 3$; (*b*) 4; (*c*) 5; (*d*) 6; (*e*) 7; (*f*) 8.

spacing are about the same. This gives the interpretation of the vortex blob size as a measure of the resolution of the interface. In the problem at hand, where the interface would be intricately mixed by small-scale turbulence, we interpret the vortex blob parameter to be the scale of local averaging of the turbulent flow, and we will use a rather large value.

Except for Dahm *et al.* (1989), whose axially symmetric case was not detailed, previous computations by the vortex blob method have been two-dimensional. Therefore we have to decide how to desingularize the kernels in this axially symmetric application. The kernels in (3.1) and (3.2) are functions of r_1 and r_2, the shortest and greatest distance from the field point to the vortex ring (they also depend linearly on $r-r'$, $r+r'$ and $z-z'$). We desingularize these kernels by replacing r_1 and r_2 by

$$r_1 = [(r-r')^2+(z-z')^2+\delta^2]^{\frac{1}{2}}, \tag{3.10}$$

$$r_2 = [(r+r')^2+(z-z')^2+\delta^2]^{\frac{1}{2}}, \tag{3.11}$$

where δ is the vortex blob parameter. We have included δ in r_2 for consistency when the field point is on the axis, where r_1 and r_2 should be equal. The kernels reduce to the usual two-dimensional versions for points near the vortex ring, and the modifications are unimportant at distant points.

The nodes are remeshed, sometimes at every time step, but usually every ten steps, placing them closer together when the circulation density and curvature are greater. We have done this by a method proposed by Dritschel (1988), which adjusts the density of nodes to fit any prescribed formula. Cubic splines are used for interpolation onto the remeshed nodes.

3.1. *Computations*

A series of computations is shown here which demonstrates how the model works and how it depends on the blob parameter δ. Figure 7 was computed using $\delta = 0.15$. An initially spherical parcel of unit radius is dropped from rest with its centre initially 3.71 units above the ground. (This makes the initial centre of gravity the same as in the 3 in. series experiments.) In the six frames shown we can see the rollup of the vortex ring as the parcel falls. The heavier fluid develops a slip-surface at its sides by baroclinic vorticity generation, i.e. from (3.5). This vortex sheet is confined to the density interface and the circulation which develops causes large deformation of this interface, resulting in the penetration of ambient fluid into the top of the heavier fluid with quite a large downdraught velocity and the formation of a vortex ring. In the early stages the downflow is in the heavier fluid, but as the vortex ring develops the downward momentum is transferred to the penetrating ambient fluid. While the parcel is still aloft the vortex ring begins to cause an outflow below, but the most important observation is the entrainment of ambient fluid into a swirl within the heavier fluid. This rollup continues after the microburst reaches the ground. As the vortex stretches along the ground the vorticity in the core is intensified by the stretching, but this is not noticeable in the figures because the core continues to grow by winding. The velocity field is partly that of a finite-core vortex ring but has quite a bit of vertical shear due to the vorticity at the inner side of the density interface.

To investigate the effect of δ we have repeated the computation with $\delta = 0.1$ and 0.05. The results are compared in figure 8 at $T/T_0 = 4$. What one sees in the figure is a rapid increase in the number of turns in the primary rollup at δ is decreased (figure 8*b* required 199 nodal points). However, there is little effect on the local velocity field in and near the vortex core, which resembles solid-body rotation at all δ. The biggest

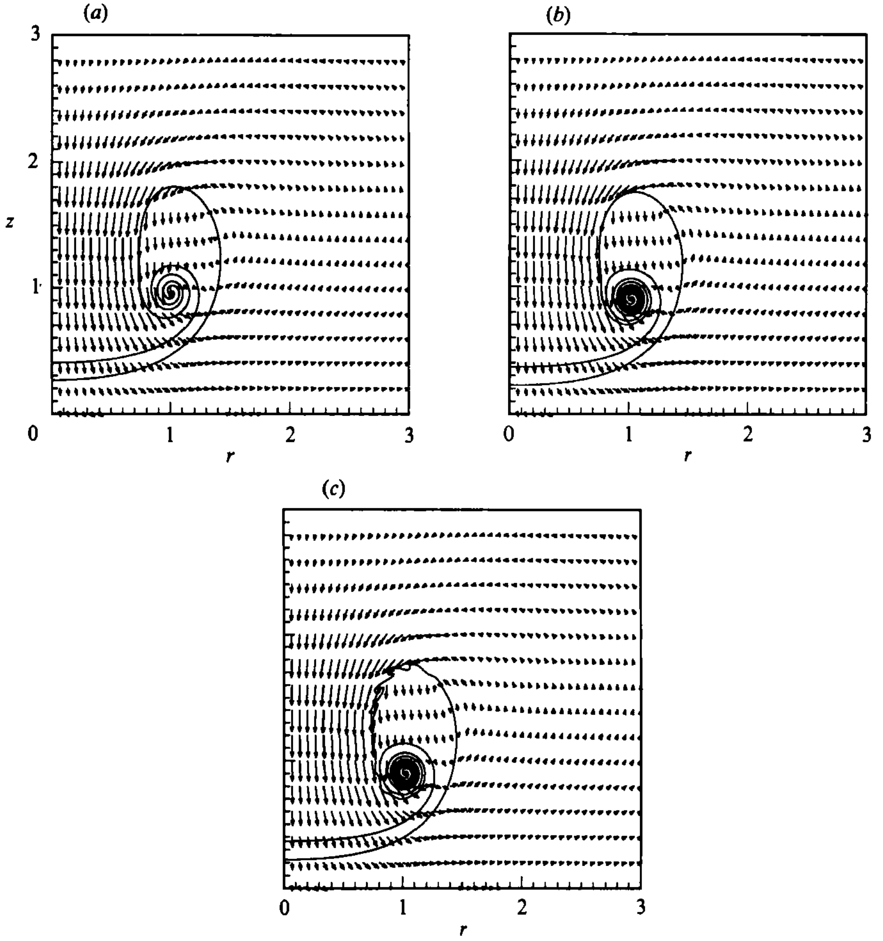

FIGURE 8. Same as figure 7 at $T/T_0^{-1}4$ showing the effect of changing the δ-parameter. (*a*) $\delta = 0.10$; (*b*) $\delta = 0.05$; (*c*) $\delta = 0.05$ with initial disturbance spectrum.

effect on the velocity field occurs across the inside edge of the vortex sheet boundary. As δ is made smaller the variation in velocity becomes sharper as the thickness of the vortex layer decreases. In the thinnest case (figure 8*b*) the vortex sheet is actually unstable; we see no disturbances because none were excited by the flow nor by the numerical scheme. To show this we ran the $\delta = 0.05$ case again with a wavy disturbance on the initial spherical surface. We introduced a spectrum of radial cosine disturbances with wavenumbers between 16 and 96 ($\cos n\theta$, n = wavenumber) each with extremely small radial amplitudes of 10^{-7} units. This result, computed with 399 nodes, is shown in figure 8*c*. The rollup of unstable Helmholtz vortices occurs where the strength of the vortex sheet is greatest. When we compute for a longer time the complexity rapidly becomes too great to resolve with this many nodes. We have effectively produced a thicker interface from the growth of vortex sheet instabilities. It is our point of view that by computing with a larger δ we simulate the effect of averaging over these 'turbulent' fluctuations. The same initial disturbance with $\delta = 0.15$ produced no instabilities with the spectral initial condition.

There are several issues which we regard as problems with this model. Even with δ as large as 0.15 the duration of the computation is limited by the number of nodes required to describe the rollup of the vortex core. With 121 nodes we cannot integrate beyond $T/T_0 = 8$. (This only takes 15 s on a Cray YMP.) We can integrate to $T/T_0 = 10$ with 399 nodes. (This takes 100 s to compute.) Too many nodes are wasted describing the fine details as the interface winds up in weaker and weaker sheets, yet the velocity field is not very complicated. We have no solution for this, it is inherent to the method.

3.2. *Surface friction*

The second problem is of a more physical nature. It is apparent on comparing figure 1 with figure 7 that the computed vortex flattens to the ground too rapidly in the last few frames. The experimental microburst maintains its height (against gravity) during late times of the outflow. We believe the flattening is caused by the neglect of surface friction. This is confirmed by Proctor (1988) who included a Navier–Stokes computation without surface friction which had this property. The effect of surface friction is to produce counter-vorticity in a turbulent boundary layer. This vorticity is swept forward and upward along the gust front as noted earlier. The effect of this is two-fold. First, the opposite-signed vorticity decreases the overall circulation and thus decreases the large outflow velocity near the ground. Secondly, the counter-vorticity, carried ahead of the main vortex, induces an upward velocity on the main vortex and elevates the head of the vortex structure. Both effects cause the vortex to slow down. In a vortex dynamics description of this essentially inviscid process, the forward motion of the vortex is caused by the interaction of the vortex with its image below the ground. Decreasing the circulation and increasing the elevation both retard the forward motion.

The interaction of *single-density* laminar vortex rings with a solid boundary is similar to the description above but they have a greater rebound than we have observed. This has been studied experimentally by Walker *et al.* (1987) and by means of two-dimensional numerical simulations by Orlandi (1990).

To simulate the effect of surface friction in the model we have allowed the circulation density to be modified by contact with the ground. We think of the no-slip boundary condition as producing a vortex sheet along the ground with circulation density equal to the slip surface velocity. Of course the image vortex sheet below the ground has the opposite sign and cancels its effect. Further, as long as the vortex sheet is on the ground it cannot be carried upward because the vertical velocity is zero there. However, small-scale turbulence near the ground would cause the vortex sheet to thicken into a vortex layer (a turbulent boundary layer). As the vorticity diffuses upward it sees an increasingly large upward velocity component which lifts it further upward where it is not completely cancelled by its image. In Proctor's computation this forms an upward penetrating vortex layer somewhat behind the gust front. In our experiments it appears to be *at* the front. In our numerical simulation we cannot introduce any new vortex sheets, so we allow this vorticity to be part of the original vortex sheet, and we introduce it into the vortex sheet a small distance above the ground, simulating the thickness of the boundary layer. We do this as follows. We first identify when the microburst is on the ground by noting when $z_0 < \delta_1$, where z_0 is the height of the lower centreline node and δ_1 is a small number. Then we identify the node j where the interface separates upward from the ground by the criterion $z(j) > \delta_2$, where $\delta_2 > \delta_1$. We assume that the circulation density along the part of the interface between j and j_0 is equal to the radial surface velocity v_r. Of course most of this vortex sheet is on the ground and has no effect. Only the part which sticks up to δ_2 can have an effect, but as time passes the nodes identified at earlier time steps are carried further upward. In the formalism it is μ

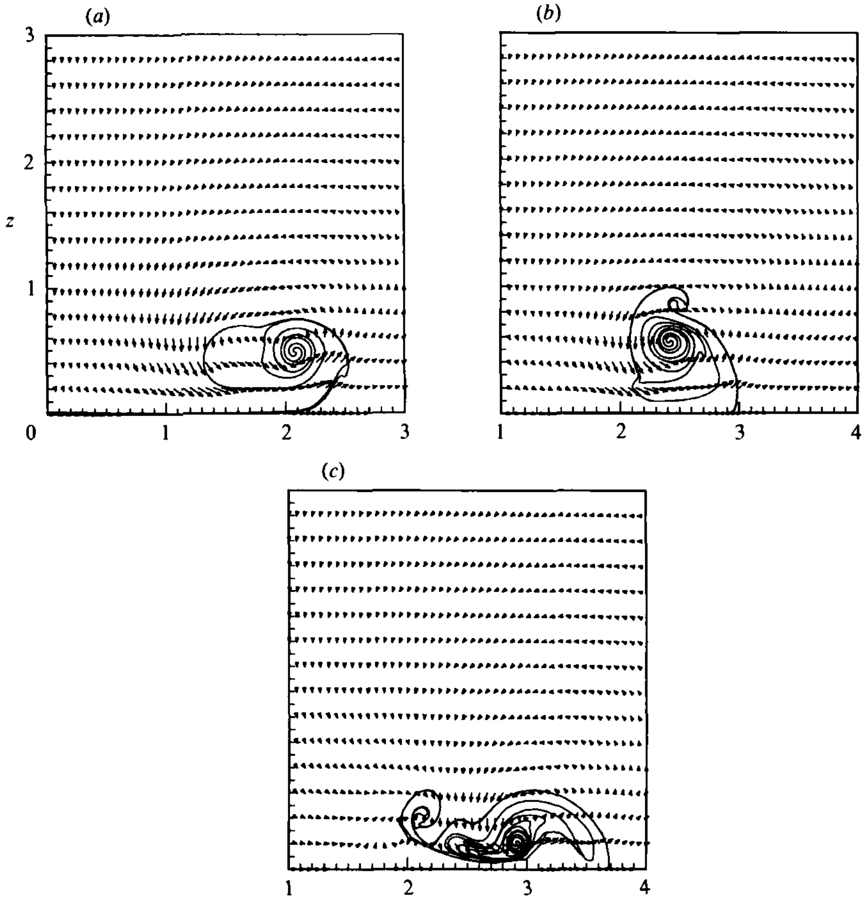

FIGURE 9. Same as figure 7 with surface friction; (*a–c*) should be compared with figure 7 (*d–f*).

which must be specified, therefore using (3.7) we compute μ as the integral of γ for each of the nodes between j and j_0, i.e.

$$\mu(j) = \mu(j_0) - \int_j^{j_0} v_r \, \mathrm{d}s. \tag{3.12}$$

This is done after each time step, replacing the old μ-values for each node which satisfies the criterion. As time proceeds some of these modified nodes are carried upward beyond the separation point. The μ-values for these are updated by (3.5) in the usual way.

We have computed with this scheme using $\delta_1 = 0.10$ and $\delta_2 = 0.15$. The results are shown in figure 9. In figure 9(*a*) one can see the first burst of counter-vorticity producing a curl on the interface. Comparing the results frame by frame with figure 7 at the same times it is clear that the modified vortex is slower and taller. A striking result is the comparison of figure 9(*c*) with the experiment in figure 1(*e*) where the reversed circulation 'rooster tail' is a dominant feature in both figures. These surface friction results are sensitive to the value assumed for δ_2. It would be desirable to relate δ_2 to an estimate of the boundary-layer thickness. However, we decided to try to keep things simple. Our objective is limited to showing that the injection of counter-vorticity has the correct effect in this model.

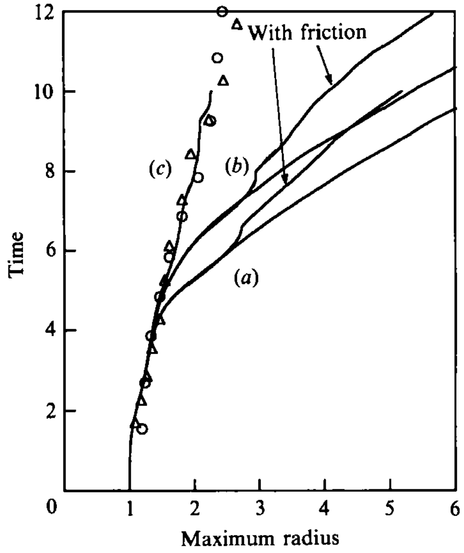

FIGURE 10. Maximum radius versus time. (*a*) Initial centre of gravity at 3.71 units, with and without friction; (*b*) initial centre of gravity at 4.65 units, with and without friction; (*c*) initial centre of gravity at 10 units compared with data from two runs (○, △) (V10905).

The maximum radius of the microburst interface, with and without surface friction, is plotted versus time from release in figures 3(*c*) and 5(*b*) in order to compare with the model experiments. In each figure the slower curve of the pair is the one with friction. Friction becomes effective quite suddenly where the curve hooks upward. It is clear from these figures that the numerical gust front advances faster than the experimental front. Including surface friction helps in this regard, as was intended. As was pointed out in §2, slightly different initial conditions would make the agreement almost perfect. These results for $3.71R_0$ and $4.65R_0$ are also shown in figure 10 along with an additional case released from $10R_0$. This high-release case, which is essentially without ground effect, corresponds to a thermal. This will be discussed later.

In figure 11 a series of surface profiles, for $3.71R_0$, is shown with and without surface friction. The plots show the radial velocity at the ground versus radial position at selected times after release. Surface velocity, which is obscured on the vector plots, is the quantity of most interest for aircraft safety. The figure shows that surface friction has the expected effect. It decreases the forward velocity of the vortex as may be seen by comparing the positions of the peaks in figure 11(*a*, *b*) at the same times, and it also decreases the values of the peak velocities. The negative surface velocities which are seen in figure 11 occur under the 'rooster tail' at times later than those shown in the vector plots and appear to be excessive. We are pushing the computation to its limit at late times in this figure so these negative velocities have smaller reliability. Experimental verification of negative velocities would be desirable.

The important physics which one should note from figure 11(*b*), and from figure 13, for the 4 in. series, is that several time units after touchdown the maximum surface velocity is about four times the velocity of advance of the vortex. This is what one would estimate from a model of a line vortex advancing in the velocity field of its image below the ground.

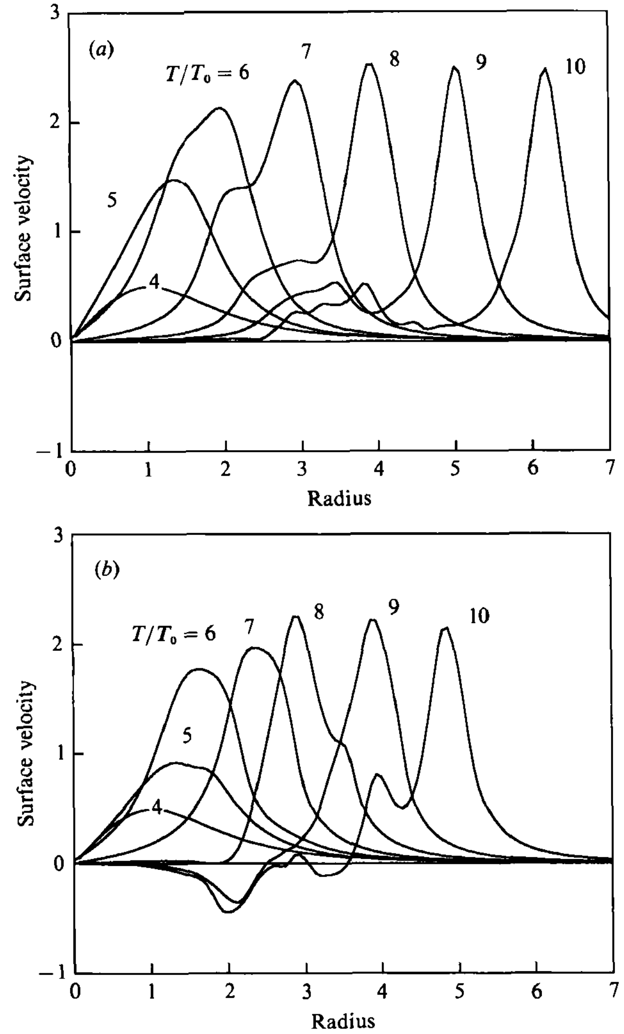

FIGURE 11. Surface velocity versus dimensionless radial coordinate at selected times for initial centre of gravity at 3.71. (a) Without friction; (b) with friction.

3.3. *Insensitivity to initial height*

We have found that these results are approximately independent of the release height. Figure 12 shows vector plots of a microburst released from $4.65R_0$ (corresponding to the 4 in. series), with surface friction. Comparison with figures 7 and 9 shows that the figures do not correspond time by time; however, at times when the fronts are at about the same radial positions (which occurs approximately one time unit later for the $4.65R_0$ case, compare figures 12 (*a–c*) with 7 (*a–c*) and figure 12 (*d–f*) with 9 (*a–c*)), they look similar. A similar observation may be made by comparing the $4.65R_0$ surface velocity plots in figure 13 with those in figure 11 (*b*). In figure 10 a shift by one time unit gives approximate coincidence of the $3.71R_0$ and $4.65R_0$ cases, and this is also approximately true in the model experiments shown in figures 3 (*c*) and 5 (*b*).

The reason for this similarity is that the circulation around the descending vortex ring develops rapidly (in about 3 time units) to a constant value while the microburst is still aloft for these cases. The vortex then proceeds with constant strength, and has

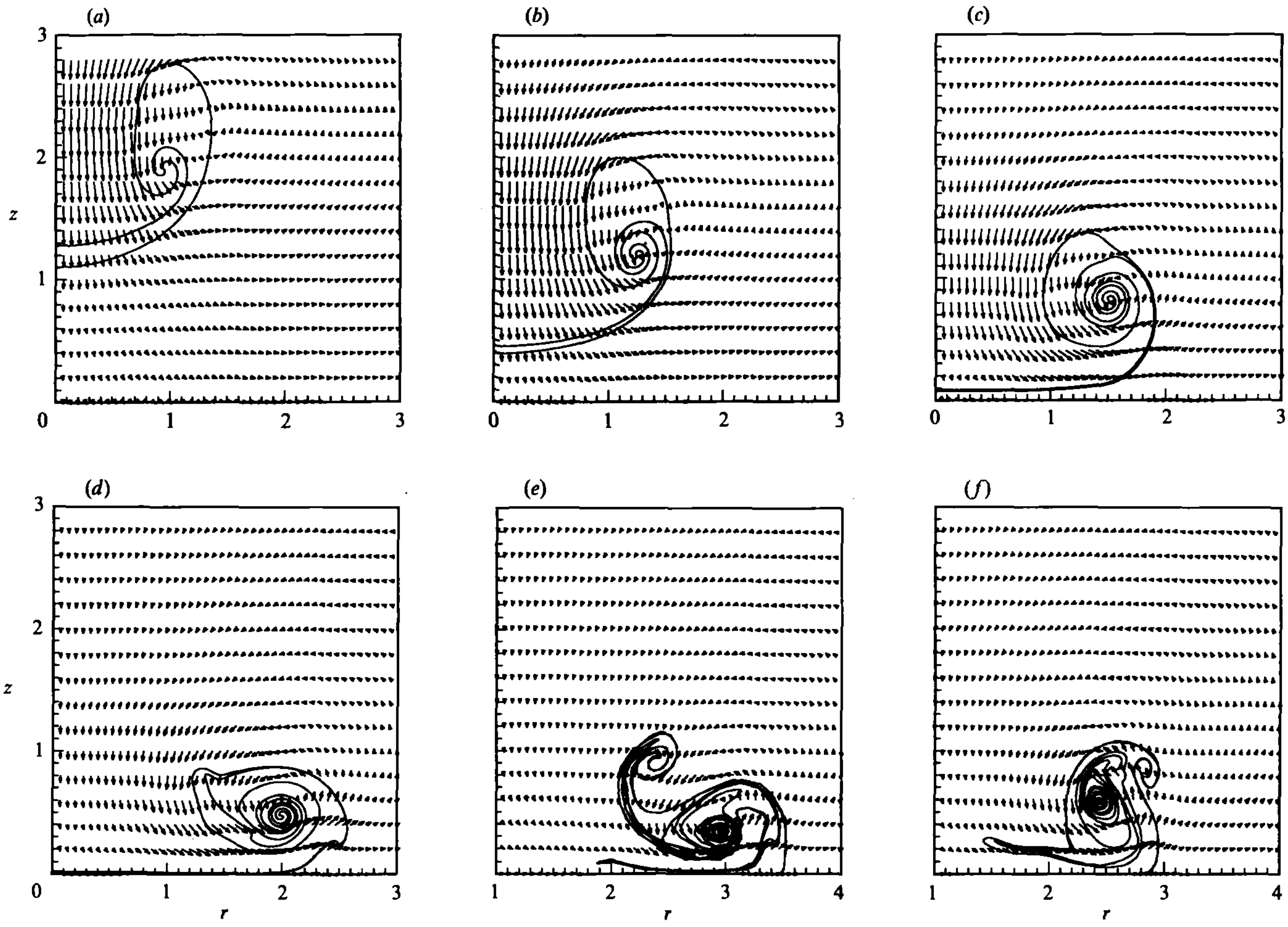

FIGURE 12. Vector plots of numerical microburst, $\delta = 0.15$, with friction. Initial centre of gravity is 4.65 units (corresponding to the 4 in. series) (*a*) $T/T_0 = 4$; (*b*) 5; (*c*) 6; (*d*) 7; (*e*) 8; (*f*) 9.

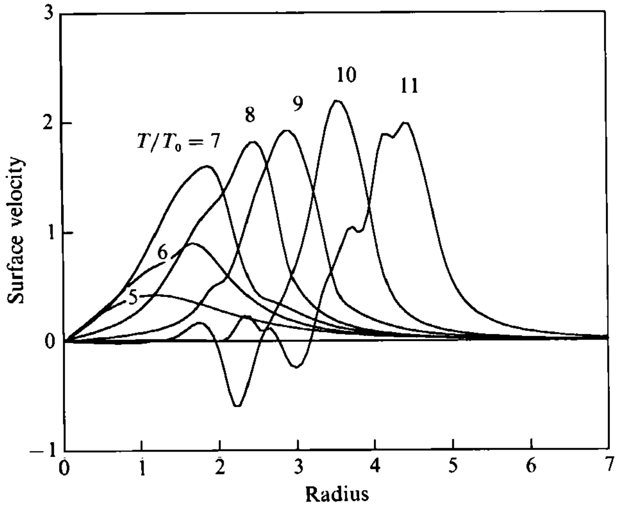

FIGURE 13. Surface velocity for 4.65 initial centre of gravity, with friction at selected times.

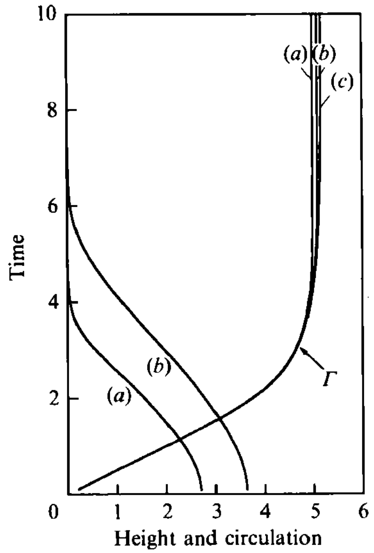

FIGURE 14. Dimensionless circulation and distance to the ground versus time. (a) Initial centre of gravity 3.71; (b) 4.65; (c) 10.00.

a nearly constant velocity until it nears the ground. This may be seen in figure 14 where the circulation as a function of time and the distance above ground are shown. The curves labelled Γ are the dimensionless circulation around the developing vortex, evaluated from the difference in the dipole density μ between the bottom and the top of the interface at the centreline. Three cases are shown: 3.71, 4.65 and 10.00 are the initial dimensionless elevations of the centres of gravity of the microbursts. The third case is initially high enough that it is essentially without ground effect for the time range shown. The circulations are nearly the same for all three cases, with final values between 5 and 5.2 units. On the same figure we show the distance of the bottom of the interface above the ground to emphasize that the circulation develops while the microburst is aloft. These curves also show portions with approximately constant velocity of descent. One should also note from figure 10 that after the circulation reaches its asymptotic value, but before the microburst touches ground, the radius of the microburst increases approximately linearly with time. This causes the noticeable linear regions on the radius profiles before touchdown. In the absence of ground effect the radial growth would remain linear for a longer time. The experimental points on figure 10 confirm this for the high-release case. The difference between two microbursts released from different heights (but not too different), and observed after full development at the same distance above the ground, is a small difference in radius and a different amount of winding in the core; the circulations and general dispositions are about the same. It follows that their future motions will be similar.

A linear increase in radius was observed in computations with vortex ring bubbles (Lundgren & Mansour 1991). A buoyant vortex ring develops naturally from a released spherical gas bubble, in a manner similar to the microburst, with a jet of liquid penetrating through the bubble from behind to form a torroidal bubble of constant circulation. The dimensionless circulation that develops is about the same as for the microburst, about 5.6 when the bubble is large enough to neglect surface tension. (The length- and timescales are the same as for the microburst but with $\Delta\rho/\rho = 1$. The Boussinesq approximation was not used for the bubble computation.)

The radial spreading seen in figure 10, especially for the high-release case, can be explained by vortex dynamics as in the bubble paper, by balancing the downward excess weight by an upward Kutta–Joukowski lift. Kutta–Joukowski lift is the perpendicular force on a vortex in a crossflow. In this case the crossflow velocity is the radial velocity v_r of the vortex ring and the force balance gives $\rho v_r \Gamma = w$, where w, the excess weight per-unit-length of vortex core, is given by

$$2\pi R_v w = \tfrac{4}{3}\pi R_0^3 g \Delta\rho, \tag{3.13}$$

R_v being the radius of the vortex ring. This balance gives

$$v_r = \frac{2}{3}\frac{R_0^3}{R_v \Gamma} g \frac{\Delta\rho}{\rho} \tag{3.14}$$

or, in dimensionless form

$$v_r = \frac{2}{3}\frac{1}{R_v \Gamma}. \tag{3.15}$$

This rate of spreading, of about $\Delta R_v = \frac{2}{15}$ per unit of time, corresponds closely to that seen in figure 10.

The high-release case corresponds to model thermal experiments performed by Scorer (1957). Scorer followed the motion of a released dense solution by taking motion pictures in a manner similar to our experiments, but for a longer period of time, and his emphasis was on long-time behaviour. He made no note of an early stage in which the spreading was linear in time. The results shown in (3.14) is the same as obtained by Turner (1957) by the impulse method described in the introduction which resulted in (1.8).

4. Comparison with microburst observations

Wilson *et al.* (1984) have studied the data from a Doppler radar network near Denver and identified and examined about 70 microbursts which occurred during the summer of 1982. They have distilled from this data the chronology and characteristics of an 'average' microburst, which we list below in a form interpreted for axially symmetric flow. The time t_i below is the time that divergent surface outflow first became apparent on the radar system.

$t_i - 5$ min: the downdraught is above 2 km, no divergence;
$t_i - 2$ min: the downdraught is below 1 km and has begun to diverge horizontally, roll vortices may be present;
t_i min: the downdraught speed has increased to about 10 m/s, the downdraught radius is 0.5 km, the maximum radial velocity is 6 m/s located 0.9 km from the centre;
$t_i + 5$ min: the divergent outflow has spread horizontally and the maximum radial velocity has peaked at 12 m/s at a radial position of 1.6 km;
$t_i + 10$ min: the horizontal flow has weakened and spread to a radius of 3–4 km.

The maximum surface velocity doubles to its peak in about 5 minutes. The peak value is about 20% larger than the earlier maximum downdraught velocity.

This information can be used to calibrate the numerical model for an 'average' microburst. The radius of the downdraught in the model is about R_0 and the maximum downdraught velocity is about $2R_0/T_0$. Using 0.5 km and 10 m/s for these values, noted at t_i, we establish $R_0 = 0.5$ km and $T_0 = 100$ s.

We can use this scaling to compare the outflow characteristics predicted by the model with the 'average' microburst. The peak radial velocity in the model is $2.2R_0/T_0$ at a radius of $3.5R_0$. (This occurs at $T/T_0 = 8.5$ for the 3.71 case and at $T/T_0 = 10$ for the 4.65 case, both with friction.) Using the scaling established above this gives a peak velocity of 11 m/s at 1.75 km which compares with the values 12 m/s at 1.6 km noted at $t_i + 5$ min. The time t_i which is 5 min earlier, or 3 time units earlier with $T_0 = 100$ s, corresponds to $T/T_0 = 5.5$ for 3.71 and to $T/T_0 = 7$ for 4.65. The results differ a bit for these two cases. For 3.71 we find the maximum velocity is 1.3 units at a distance of 1.5 units corresponding to 6.5 m/s at 0.75 km, while for 4.65 we find the maximum velocity is 1.6 units at a distance of 2 units or 8 m/s at 1 km. The 'average' microburst has 6 m/s at 0.9 km. The differences here are relatively small if one takes into account that the surface velocity is changing very rapidly with time in this range and the result depends strongly on the estimate for T_0. The model has done remarkably well for these comparisons because we have determined the scaling so that the numerical results agree with early time observations instead of determining the scaling to agree with our experiments as we did for the DL 191 comparison.

5. Conclusions

A simple microburst model consisting of a single released volume of heavier liquid falling onto a horizontal plane was investigated experimentally and numerically. Two geometrically similar microburst flows with different values of $\Delta\rho$ develop at different rates, the one with the larger $\Delta\rho$ falling faster. An inviscid scaling law which absorbs $\Delta\rho$ and gravity into the timescale was used for comparing such flows.

Experimentally simulated microbursts, using salt water releases into fresh water, had good repeatability if care was taken when piercing the retaining membrane. Results for the radius of the microburst gust front, taken from video recordings of the events, compared well when scaled with the length- and timescales proposed and were found to be independent of Reynolds number when it was larger than 3000.

These results were compared with data from the DL 191 microburst (Fujita 1986) to establish an effective scaling of $R_0 = 0.7$ km and $T_0 = 23$ s for this microburst.

A numerical model, based on inviscid vortex dynamics, gave a detailed picture of the development of a microburst which supplements our incomplete measurements. As the heavier fluid begins to accelerate downward a strong shear layer forms between it and the lighter fluid which rises around it. The vorticity in this shear layer forces lighter fluid to penetrate through the heavier fluid from above, forming a heavy-fluid vortex ring which entrains lighter fluid by winding. In this process, the heavier fluid at first gains momentum by accelerating in the gravitational field, but as the vortex develops, momentum is transferred to the lighter fluid until it mostly resides in a vigorous downflow of lighter fluid through the aperture of the vortex ring. The circulation about the vortex ring rapidly increases, reaching a constant value

$$\Gamma = 5R_0^2/T_0, \tag{5.1}$$

while the microburst is still aloft. This causes the vortex to descend with a nearly constant velocity (until it gets too close to the ground) while spreading its radius approximately linearly with time, gaining momentum by increasing its mass instead of accelerating.

If we use the effective scaling of DL 191 noted above we estimate the circulation of that microburst to be $\Gamma = 0.11$ km^2/s. This is a measure of its strength.

We compared the numerical results with the properties of an 'average' microburst extracted by Wilson *et al.* (1984) from Doppler radar return data from 70 microbursts observed near Denver in 1982. Gross features such as the relationship of the peak outflow velocity to the maximum downdraught velocity, the radial position of the peak outflow velocity and the time required for the maximum outflow velocity to double were in agreement. The scaling for the 'average' microburst was $R_0 = 0.5$ km and $T_0 = 100$ s. The circulation of the 'average' microburst is thus $\Gamma = 0.0013$ km^2/s, much weaker than DL 191.

This work was supported by NASA-Ames Research Center, through a NASA-Ames University Consortium Agreement, contract NCA2-329. We also acknowledge a grant from the University of Minnesota Graduate School.

REFERENCES

Abramowitz, M. & Stegun, I. A. 1972 *Handbook of Mathematical Functions*. Washington, DC: Government Printing Office.

Dahm, W. J. A., Scheil, M. & Tryggvason, G. 1989 Dynamics of vortex interaction with a density interface. *J. Fluid Mech.* **205**, 1–43.

Dritschel, D. G. 1988 Contour surgery: a topological reconnection scheme for extended integrations using contour dynamics. *J. Comput. Phys.* **77**, 240–266.

Fujita, T. T. 1981 Tornadoes and downbursts in the context of generalized planetary scales. *J. Atmos. Sci.* **38**, 1511–1534.

Fujita, T. T. 1985 *The Downburst*. The University of Chicago Press.

Fujita, T. T. 1986 *DFW Downburst*. The University of Chicago Press.

Higdon, J. J. L. & Pozrikidis, C. 1985 The self-induced motion of vortex sheets. *J. Fluid Mech.* **150**, 203–231.

Ivan, M. 1986 A ring-vortex downburst model for flight simulation. *J. Aircraft* **23**, 232–236.

Krasny, R. 1987 Desingularization of Periodic Vortex Sheet Rollup. *J. Comput. Phys.* **65**, 292–313.

Lamb, H. 1932 *Hydrodynamics*, Cambridge University Press.

LEONARD, A. 1985 Computing three-dimensional flows with vortex elements. *Ann. Rev. Fluid Mech.* **17**, 523–559.

LUNDGREN, T. S. & MANSOUR, N. N. 1991 Vortex ring bubbles. *J. Fluid Mech.* **224**, 177–196.

MAXWORTHY, T. 1972 The structure and stability of vortex rings. *J. Fluid Mech.* **51**, 15–32.

MAXWORTHY, T. 1974 Turbulent vortex rings. *J. Fluid Mech.* **64**, 227–239.

MEIRON, D. I., BAKER, G. R. & ORSZAG, S. A. 1982 Analytical structure of vortex-sheet dynamics. Part 1. Kelvin–Helmholtz instability. *J. Fluid Mech.* **114**, 283–298.

MOORE, D. W. 1979 The spontaneous appearance of a singularity in the shape of an evolving vortex sheet. *Proc. R. Soc. Lond.* A **365**, 105–119.

ORLANDI, P. 1990 Vortex dipole rebound from a wall. *Phys. Fluids* A **2**, 1429–1436.

POZRIKIDIS, C. & HIGDON, J. J. L. 1985 Nonlinear Kelvin–Helmholtz instability in a finite vortex layer. *J. Fluid Mech.* **157**, 225–263.

PROCTOR, F. H. 1988 Numerical simulations of an isolated microburst. Part I: Dynamics and structure. *J. Atmos. Sci.* **45**, 3137–3160.

SCORER, R. S. 1957 Experiments on convection of isolated masses of buoyant fluid. *J. Fluid Mech.* **2**, 583–594.

SIMPSON, J. E. 1972 Effects of the lower boundary on the head of a gravity current. *J. Fluid Mech.* **53**, 759–768.

TRYGGVASON, G. 1989 Simulations of vortex sheet rollup by vortex methods. *J. Comput. Phys.* **80**, 1–16.

TURNER, J. S. 1957 Buoyant vortex rings. *Proc. R. Soc. Lond.* A **239**, 61–75.

WALKER, J. D. A., SMITH, C. R., CERRA, A. W. & DOLIGALSKI, T. L. 1987 The impact of a vortex ring on a wall. *J. Fluid Mech.* **181**, 99–140.

WILSON, J. W., ROBERTS, R. D., KESSINGER, C. & MCCARTHY, J. 1984 Microburst wind structure and evaluation of Doppler radar for airport wind shear detection. *J. Climate Appl. Met.* **23**, 898–915.

ZHU, S. & ETKIN, B. 1985 Model of the wind field in a downburst. *J. Aircraft* **22**, 595–601.